A method for identifying the boundary of regions in welded coupon specimens using digital image correlation

Yan, Rui; El Bamby, Hagar; Veljkovic, Milan; Xin, Haohui; Yang, Fei

DOI
10.1016/j.matdes.2021.110073

Publication date
2021

Document Version
Final published version

Published in
Materials and Design

Citation (APA)
Yan, R., El Bamby, H., Veljkovic, M., Xin, H., & Yang, F. (2021). A method for identifying the boundary of regions in welded coupon specimens using digital image correlation. *Materials and Design*, *210*, Article 110073. https://doi.org/10.1016/j.matdes.2021.110073

Materials & Design 210 (2021) 110073

Contents lists available at ScienceDirect

Materials & Design

journal homepage: www.elsevier.com/locate/matdes

A method for identifying the boundary of regions in welded coupon specimens using digital image correlation

Rui Yan [a,*], Hagar El Bamby [a], Milan Veljkovic [a], Haohui Xin [b], Fei Yang [a,c]

[a] Department of Engineering Structures, Delft University of Technology, Delft, the Netherlands
[b] Department of Civil Engineering, Xi'an Jiaotong University, Xi'an, China
[c] Department of Bridge Engineering, Tongji University, Shanghai, China

HIGHLIGHTS

- The slop of minor-major strain relationship reveals the internal transverse constraint in a butt-welded coupon during tensile loading.
- The HAZ boundary is identified by the slop of the minor-major strain relationship.
- 'V' and 'monotonic' shapes of the slop distribution along the loading direction exist in the HAZ region.
- The HAZ boundary identified by the slop of the minor-major strain relationship is verified by hardness and microstructure results.

GRAPHICAL ABSTRACT

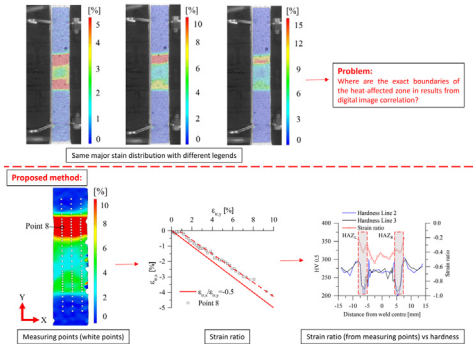

ARTICLE INFO

Article history:
Received 2 July 2021
Revised 16 August 2021
Accepted 24 August 2021
Available online 25 August 2021

Keywords:
Welded coupon test
Transverse butt weld
Digital image correlation
Heat-affected zone

ABSTRACT

The coupon specimen with a transverse butt weld in the middle could be used for determining local constitutive properties of the heat-affected zone (HAZ) and the weld metal (WM) based on the digital image correlation (DIC). However, limited research is reported to demonstrate how to identify the boundary of each region in DIC results. Accordingly, it is difficult to determine the adequate gauge length for measuring the strain of each region and establishing a stress–strain curve for Finite Element Analysis (FEA) of structural problems. In this paper, a method for identifying the region's boundary is proposed based on coupon tests using three steel grades, S355, S500, and S700, corresponding to three weld matching types, match, overmatch, and undermatch, respectively. First, the hardness and the microstructure investigation were conducted to determine the region's boundary. Then, the boundary was identified based on the DIC result using the proposed method. Finally, the identified HAZ regions were verified against hardness results. Using the proposed method, the gauge length for measuring the strain of a single region, such as HAZ and WM, are determined based on the DIC results. The primary purpose is to establish the stress–strain relationship for FEA of welded joints.

1. Introduction

Welded joints are wildly used in metal structures, such as steel structures and aluminium structures. In general, a welded joint is split into three regions, which are the base material (BM), the

* Corresponding author.
E-mail address: r.yan@tudelft.nl (R. Yan).

https://doi.org/10.1016/j.matdes.2021.110073
0264-1275/

heat-affected zone (HAZ), and the weld metal (WM) for the Finite Element Analysis (FEA) of structural problems. The material mechanical property varies in each region due to the diverse microstructures. Therefore, it is essential to know each region's stress–strain relationship to properly predict the strength, stiffness and ductility of the welded joint.

Four approaches are commonly used to obtain the local properties of a welded joint. The first approach is based on the Vickers hardness test and the empirical hardness-strength correlation [1–3]. The stress–strain relationship is generated based on the Considère's necking criterion [4] and the theoretical material constitutive model, such as the Hollomon's model [5]. The advantages of this approach are the simple testing scheme and independent testing results for each region. However, the empirical hardness-strength correlations proposed by different researchers are valid only for the investigated material. In addition, Leitao et al. [6] found that WM had a higher yield strength but a lower hardness than BM. The reason is that the indentation formed in the Vickers hardness test is associated with an approximately 8% strain, as illustrated by Tabor [7]. Therefore, the hardness result is not directly correlated to the yield strength and the ultimate strength, indicating that the stress–strain relationship cannot be accurately established only based on the Vickers hardness test. Besides, while easy to conduct, the Vickers hardness test is a rather time-consuming procedure to test a large number of indentation points across the weld.

The second approach is the micro-specimen tensile test [3,8–11]. HAZ and WM micro-specimens were fabricated from the weld region [3,9–11]. Alternatively, Amraei et al. [8] applied thermal cycles on steel plates using a thermal simulation machine. The thermal cycles followed the temperature–time history in the material at various distances from the weld bead in a typical gas metal arc welding process. The micro-specimen was fabricated from the heat-treated plates representing different HAZ sub-regions. A rather accurate stress–strain relationship could be obtained by this approach, provided that the tested material in the micro-specimen is homogeneous. However, it is difficult to ensure the homogeneity of the material since steep gradients in material properties may exist in the sub-regions. In addition, the fabrication and testing of the micro-specimen are very complicated.

The third approach is to simulate the welding process by the Thermal-mechanical FEA [12,13]. The highest temperature in history was recorded in each element in the thermal Finite Element Model (FEM). And the corresponding material property, depending on the highest temperature, was assigned to each element in the mechanical FEM. The welded coupon test was conducted to validate the FE model. Nevertheless, the welding heat input and the cooling rate play key roles in the microstructure and consequently in the mechanical performance of the material [14–16]. Therefore, the material property depending on the highest temperature is not suitable for WM and HAZ.

The fourth approach is to conduct the tensile test on the coupon specimen with a butt weld in the middle transverse to the loading direction, using the digital image correlation (DIC) technique [6,17–25]. DIC is a non-contact technique for the surface strain measurement. Compared with other approaches for obtaining local properties, DIC could be used to measure the local deformation in each region from a single tensile experiment. It was initially used by Peters and Ranson [26] in the 1980 s. Reynolds and Duvall [17] obtained the local properties of regions based on the uniform stress assumption. Lockwood et al. [18] validated the approach and uniform stress assumption for local material properties proposed in [17] by the two-dimensional (2D) FE analysis. The predicted stress was higher than the experimental result at the same deformation level. The reason was demonstrated in [19], where the plane stress and the plane strain conditions were compared to the experiment and the three-dimensional (3D) FE model. It was found that nearly plane stress conditions existed in the specimen while a plane strain condition was used in [18]. Besides, the yield strength of different regions in the thick (around 8 mm) specimen and the thin (2.5 mm, milled from the thick specimen) specimen were compared in [19]. The yield strength of the material in the thin specimen was lower in HAZ and higher in the rest regions than that of the thick specimen, indicating that the constraint in the thickness direction exists in the thick specimen. Therefore, it is essential to use a thin specimen in the coupon test to eliminate the constraint in the thickness direction. Sutton et al. [20] proposed the virtual fields method and compared it to the uniform stress method. The same assumptions, which were the plane stress condition and the regions arranged in series, used in the uniform stress method were adopted in the virtual fields method. A very good agreement was obtained between the results from the two methods. Leitao et al. [6] conducted tensile tests on coupons with transverse weld and longitudinal weld. A transverse constraint was observed in the coupon with the transverse weld since the slope of the minor strain-major strain relationship differed from −0.5. It was also found that the constraint has negligible influence on the established stress–strain relationship, comparing the results from the coupons with the longitudinal and the transverse weld. Li et al. [24] proposed a two-step procedure for determining the strain hardening exponent n using DIC measurement and the strength coefficient K using the inverse modelling procedure. The identified material parameters were validated against the load-depth relationship of indentation obtained from the hardness test.

Although many researches have been carried out on the material property investigation using the fourth approach [6,17–25], the paper demonstrating how to obtain the deformation from each region is rare. It is indeed possible to extract strain from a single facet point. However, a single point cannot represent the material of the whole HAZ, considering the heterogeneity of HAZ. Moreover, the strain from a single facet point may contain some noise which has a significant influence at the elastic stage and the onset of yielding. Therefore, it is necessary to obtain the strain of each region based on a virtual extensometer with a certain gauge length in DIC. A question arises on how to determine the gauge length for each region.

Fig. 1 presents an example of the major strain contour plot of an S700 welded coupon tested in this study. The figures are generated based on 3D DIC results at the ultimate load. The only difference among these figures is the maximum strain value used in the legend, e.g. the refinement level of the contour plots. Two high strain stripes corresponding to two HAZs exist in each figure. The width of the red colour stripe decreases with the increase of the maximum strain in the legend. Therefore, the HAZ boundary cannot be determined by the colour (width of the maximum strain strip), consequently by the magnitude of the strain used for the contour plot. Additionally, Lockwood and Reynolds [19] conducted experiments on coupons with a transverse butt weld. It was found that negative stress perpendicular to the loading direction existed in regions (WM and BM) closing to HAZ boundaries during the experiments. The negative stress would lower the yield strength of the material, resulting in the mitigation of the strain localisation. BM and WM adjacent to HAZ may have a larger strain than the material far from the boundary. Hence, it is difficult to distinguish the "over-deformed" BM and WM from HAZ, especially if the strength of BM, WM, and HAZ are very close. Therefore, it is essential to develop a method for identifying the region's boundary so that the strain could be measured from the virtual extensometer within a single material region using DIC.

In the present research, tensile coupon tests were conducted on the specimen with a transverse butt weld in the middle. Three steel grades, S355, S500, and S700, corresponding to three weld match-

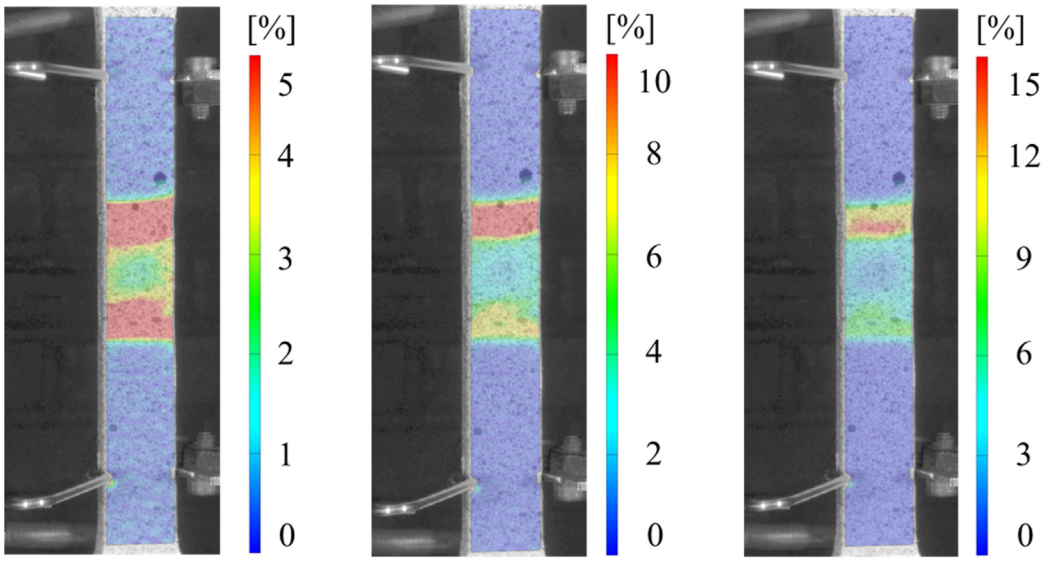

Fig. 1. Strain contour plot of an S700 welded coupon at the ultimate load with different strain legends.

ing types, match, overmatch, and undermatch, respectively, were investigated. First, the boundaries of the regions were determined using the low-force Vickers hardness test (HV 0.5) and the microstructure observation. Then, the slope of the minor strain-major strain relationship measured by 3D DIC is used to identify the boundary of HAZ. Finally, the identified boundary is verified against the hardness test results. The innovation of the proposed method is to directly identify the boundary of HAZ from a single welded coupon test using DIC without any additional metallurgical investigation. It should be used accompanying the fourth approach for obtaining the material property of regions. Since the proposed method is independent of the material category, it might be used not only for steel but also for aluminium, for example, in the case of the friction stir welded aluminium coupon.

2. Experimental program

2.1. Materials

Cold-formed square hollow sections (SHS) were used as BM in this study. The steel grades of these profiles were S355, S500, and S700. Each steel grade is examined using two nominal thicknesses, 8 mm and 10 mm, resulting in six profiles in total, as shown in Table 1. The code-name of each profile consists of the steel grade and the nominal thickness. For example, S700t8 represents the profile with S700 steel grade and 8 mm nominal thickness.

The tube ends were bevelled to a single V groove and preheated by an interpass temperature ranging from 20 °C to 200 °C to avoid hydrogen cracking. Finally, the two tubes were transversely welded using the metal active gas (MAG) welding process with a heat input varying from 1 to 1.4 kJ/mm. The filler metal Carbofil 1 was used for S355 tubes, while S500 and S700 tubes were welded with the filler metal Union Nimocr. The mechanical properties of BM and the filler metal are presented in Table 2. Note that tensile tests were conducted on standardized coupon specimens [27] with nominal thicknesses (8 mm and 10 mm) to obtain the BM property, while the fabricator provided the result of filler metal. From Table 2, it can be seen that the weld of S355, S500, and S700 coupons were match, overmatch, and undermatch weld, respectively. The nominal chemical compositions in weight percentage of the base material and the filler metal are presented in Table 3.

Table 1
Geometric property of base materials.

Code-name	Steel grade	Profile	Nominal thickness [mm]
S355t8	S355	140 × 140 × 8	8
S355t10		160 × 160 × 10	10
S500t8	S500	140 × 140 × 8	8
S500t10		160 × 160 × 10	10
S700t8	S700	120 × 120 × 8	8
S700t10		120 × 120 × 10	10

2.2. Microstructure observation and HV 0.5 hardness tests

A Small Sample perpendicular to the weld was cut out from each welded tube by the water-jet cutting, as shown in Fig. 2. The sample with 40 mm total length comprised BM, HAZ, and WM. Firstly, the sample was mounted in resins in order to ease the following polishing and etching procedures. Secondly, the testing surface was polished with SiC abrasive papers from 80 to 2000 grit and finished with MD/DP-Nap 1 μm cloth. A perfect mirror-like surface was obtained after the polishing procedure. The polished surface was etched with 2% Nital solution for 25 s. Afterwards,

Table 2
Mechanical property of the base material and filler metal.

Code-name	Yield strength [MPa]	Tensile strength [MPa]	A [%]
S355t8	506	536	27
S355t10	506	539	27
S500t8	580	617	25
S500t10	593	630	21
S700t8	789	861	14
S700t10	830	902	13
Carbofil 1	502	574	28
Union Nimocr	720	780	17

where A is the percentage elongation after the fracture based on the 5.65 coefficient of proportionality, according to [27].

Table 3
Nominal chemical composition of the base material and the filler metal [wt%].

Code-name	C	Si	Mn	P	S	Cr	Ni	Cu	Mo	Ti	Al
S355t8	0.07	0.19	1.42	0.012	0.006	0.051	0.037	0.015	0.008	0.015	0.037
S355t10	0.08	0.19	1.43	0.012	0.004	0.040	0.036	0.013	0.002	0.018	0.037
S500t8	0.06	0.17	1.21	0.010	0.004	0.044	0.037	0.012	0.003	0.002	0.031
S500t10	0.05	0.17	1.19	0.009	0.003	0.037	0.035	0.012	0.005	0.002	0.030
S700t8	0.05	0.19	1.81	0.011	0.002	0.041	0.037	0.014	0.005	0.110	0.036
S700t10	0.06	0.18	1.81	0.011	0.003	0.045	0.034	0.012	0.005	0.113	0.041
Carbofil 1	0.078	0.85	1.45	0.008	0.004	0.03	0.01	0.01	0.01	0.02	<0.01
Union Nimocr	0.09	0.61	1.71	0.005	0.01	0.19	1.47	0.03	0.51	0.06	<0.01

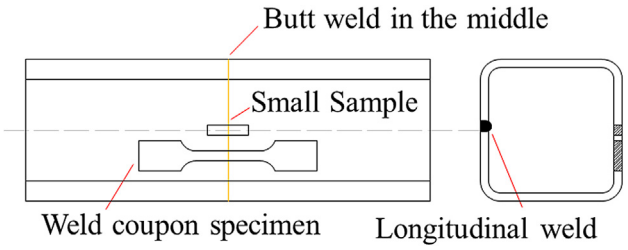

Fig. 2. Specimen cutting scheme.

the microstructure of the prepared surface was observed using a Keyence VHX-7000 digital microscope.

After the microstructure observation, the low-force Vickers hardness test (HV 0.5) was carried out following Standards [28,29], using an EMCO DuraScan 70 G5 automatic hardness tester. Four indentation lines with 28 mm total length, shown as blue lines in Fig. 3, were made on each sample. The distance from each indentation line to the top edge of the surface (Y_i) are presented in Table 4. A universal 1 mm interval of indentation was applied on each line except for HAZ, where a 0.25 mm interval was used. The boundary of HAZ shown as the orange line in Fig. 3 was determined by the observed microstructure prior to the hardness test.

2.3. Tensile coupon tests

The coupon specimen with a butt weld in the middle (welded coupon) was cut out from the opposite side of the tube's longitudinal weld, as shown in Fig. 2. One welded coupon specimen was extracted from each SHS profile, resulting in two specimens for each steel grade and six specimens in total. The specimen was milled to a central thickness zone of 3 mm to have a perpendicular HAZ boundary through the thickness. The thickness of all six tested welded coupons was 3 mm. Consequently, the uniform stress method [17] is used in this study for obtaining the engineering stress during the loading. The code-name of each welded coupon specimen is identical to its profile code-name used in Table 1.

The tensile test was carried out in an Instron tensile testing machine with 100 kN capacity. The loading controlled by the displacement was 0.01 mm/s, satisfying the loading rate requirement in [27]. The deformation during the test was measured by a 50 mm extensometer and 3D DIC (ARAMIS), as shown in Fig. 4.

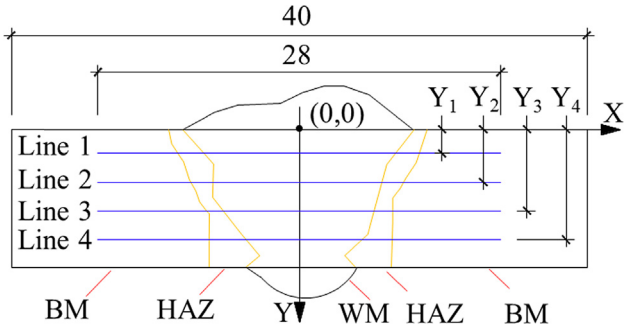

Fig. 3. Hardness testing scheme on Small Sample [mm]

2.4. DIC setup

The specimen's surface, facing the DIC camera, was prepared with a speckle pattern. The quality of the speckle has a significant influence on the accuracy of the results. Reu [30,31] suggests that the speckle size should be between 3-by-3 and 7-by-7 pixels. The imaging resolution is 67 μm/pixel (150 pixels for 10 mm) in the current research. Therefore, the ideal range of the speckle size yields in between 0.2 mm and 0.6 mm. The size of the majority sprayed speckles was between 0.2 mm and 0.3 mm in the tested specimens.

The DIC system was calibrated using the calibration panel "CP40/MV320". During the calibration, the panel was moved and rotated following the instructions from the software "GOM ARAMIS professional". The calibration was accomplished with 0.063 pixels deviation, which satisfies the required limit deviation value of 0.1 pixels. In addition, comparing the engineering strain measured by the extensometer and DIC, the maximum deviation at fracture point is less than 0.6%. This leads to the conclusion that the DIC system is properly validated.

In the data processing, the deformation of the specimen is calculated based on the motion of the subset (facet), which is a set of pixels in a square region. The number of involved pixels on one side of the square region is the subset size. Sutton [32] recommends that at least three speckles should be included in one subset in order to keep the uniqueness of each subset. Hence, a three-time speckle size (9 pixels) is employed as the subset size. Another critical dimension is the step size which is the distance between two adjacent subset centres. A 5-pixels step size is adapted, resulting in 0.34 mm of the physical dimension. The step size is smaller than the minimum interval of the strain-ratio data point (0.5 mm as illustrated in Section 3.3), indicating that the step size could satisfy the accuracy requirement of the strain ratio analysis.

3. Results and discussions

3.1. HV 0.5 hardness and microstructure results

The contour plot of the HV 0.5 hardness is presented in Appendix A, based on the hardness results from four indentation lines. The microstructure of the material in the red dash box is identified into four categories which are the base material (BM), the fine-grain heat-affected zone (FGHAZ), the coarse-grain heat-affected zone (CGHAZ), and the weld metal (WM). The typical microstructures of four regions are also presented in Appendix A. The boundary of these regions is determined based on the distinct difference of the microstructure, represented by the red dash-line. It can be seen that the determined microstructure boundaries are in good

Table 4
The distance of the indentation line from the top edge [mm].

Code-name	Y1	Y2	Y3	Y4
S355t8, S500t8, S700t8	1.5	3	5	6.5
S355t10, S500t10, S700t10	2	4	6	8

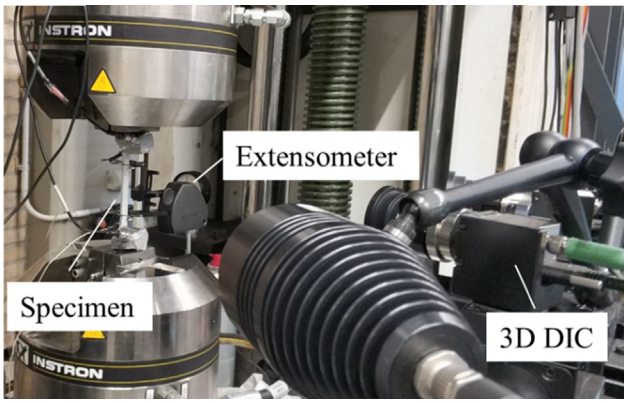

Fig. 4. Arrangement of measurements in the tensile test.

agreement with the hardness results. The lowest hardness appears in FGHAZ, which is aligned with the results in [8,12,33].

Table 5 presents the average hardness of the base material (labelled BM_{ave}), the average hardness of the weld metal (labelled WM_{ave}), and the minimum hardness of HAZ (labelled HAZ_{min}). The reason for using the minimum hardness of HAZ and the average hardness of BM and WM is that the weakest material layer in HAZ governs the strength of the coupon while BM and WM are relative homogeneous materials (which do not govern the failure mode of the specimen). BM and WM are compared to HAZ concerning the hardness difference in columns BM-HAZ and WM-HAZ of Table 5, respectively. Three combinations of the material strength difference are identified in the specimens, assuming a constant link between the hardness and the material strength in different regions of the welded specimens. Both BM and WM are slightly stronger than HAZ in S355 coupons. For S500 coupons, BM is slightly stronger, while WM is much stronger than HAZ. S700 coupons have much stronger material in BM and WM. The larger the hardness difference, the stronger the transverse constraint at the boundary of two regions. Therefore, three constraint combinations for HAZ, which are the weak-weak, weak-strong, and strong-strong constraint, could be recognized in the six tensile tests.

3.2. Tensile test results

Fig. 5 depicts the major (longitudinal) true strain distribution at the ultimate load in each test. Two regions showing high strain accompanying the necking phenomenon could be observed in all tests. It indicates that the deformation primarily concentrates on HAZ, which governs the failure.

The engineering stress–strain relationships of six tensile coupon tests are plotted in Fig. 6. The engineering strain is obtained from a 50 mm extensometer covering BM, HAZ, and WM zones, indicating that a "constant" strain is assumed along the extensometer base length. The 0.2% proof yield stress and the tensile strength are compared to BM in Table 6. Significant yield and tensile strength reductions exist in S700 welded coupons, while S355 and S500 welded coupons show much smaller (if any) strength reductions. The reduction discrepancy could be explained by the hardness results shown in Appendix A and Table 5. The strength of the welded coupon is governed by HAZ, where the lowest hardness value is obtained compared to BM and WM. The minimum hardness of S700 HAZ has the most significant hardness reduction (73 on average), while S355 and S500 grade specimens show a reduction of 23 and 37 hardness on average compared to BM, respectively.

3.3. Principal strain analysis

Leitao et al. [6] verified a linear strain path (whereby the slope of the $\varepsilon_{tr,x}$-$\varepsilon_{tr,y}$ relationship is constant in the stage beyond the yield strain, see Fig. 8) registered in the weld zone by analysing the major and minor true strains evolution. The slope of the minor true strain-major true strain relationship indicated the existence of constraints from the adjacent regions. Therefore, the principal strain analysis is conducted based on the true principal strains measured from single points in DIC. Fig. 7 shows the positions of the strain measurement points, the white squares, on the specimen S700t10. The measuring interval in HAZ is 0.5 mm, while the interval in the other regions is 1 mm. The data measured from Point 8 in HAZ is used as an example to demonstrate the analysis approach.

Since the specimen is loaded in the Y direction, the major and minor true strains are $\varepsilon_{tr,y}$ and $\varepsilon_{tr,x}$, respectively. The minor true strain-major true strain ($\varepsilon_{tr,x}$-$\varepsilon_{tr,y}$) relationship is plotted until the maximum load in Fig. 8. Considering the volume preservation assumption at the plastic stage (Equation (1)), the strain ratio $\varepsilon_{tr,x}/\varepsilon_{tr,y}$ should be equal to −0.5 in a uniaxial tensile loading condition at the plastic stage, shown as the solid red line in Fig. 8. Therefore, the principal strain ratio, which is the slope of the $\varepsilon_{tr,x}$-$\varepsilon_{tr,y}$ relationship at the plastic stage, is examined and approximated by the red dash line in Fig. 8. For simplicity, the slope of the $\varepsilon_{tr,x}$-$\varepsilon_{tr,y}$ relationship is called the strain ratio hereafter.

$$\varepsilon_{tr,x} + \varepsilon_{tr,y} + \varepsilon_{tr,z} = 0 \quad (1)$$

3.4. Finite Element analysis (FEA)

A FEA is conducted to verify the effect of the regions' boundary constraint on the strain ratio, using the ABAQUS:2019 software package [34]. Following assumptions are used in the model: 1) a sufficient length of every region is possible to distinct; 2) hardness measurements difference between adjacent regions are clear; and 3) plastic strains exist in every region. This ideal situation is introduced to illustrate the interaction between adjacent regions. The model consists of two 100 mm regions, resulting in 200 mm in total. The width and the thickness are constant, 10 mm and

Table 5
HV 0.5 hardness test results.

Code-name	BM_{ave}	HAZ_{min}	WM_{ave}	BM-HAZ	WM-HAZ	Constraint combination
S355t8	179	156	183	23	23	weak-weak
S355t10	188	166	185			
S500t8	210	164	253	37	82	weak-strong
S500t10	210	183	257			
S700t8	274	208	264	73	59	strong-strong
S700t10	298	219	282			

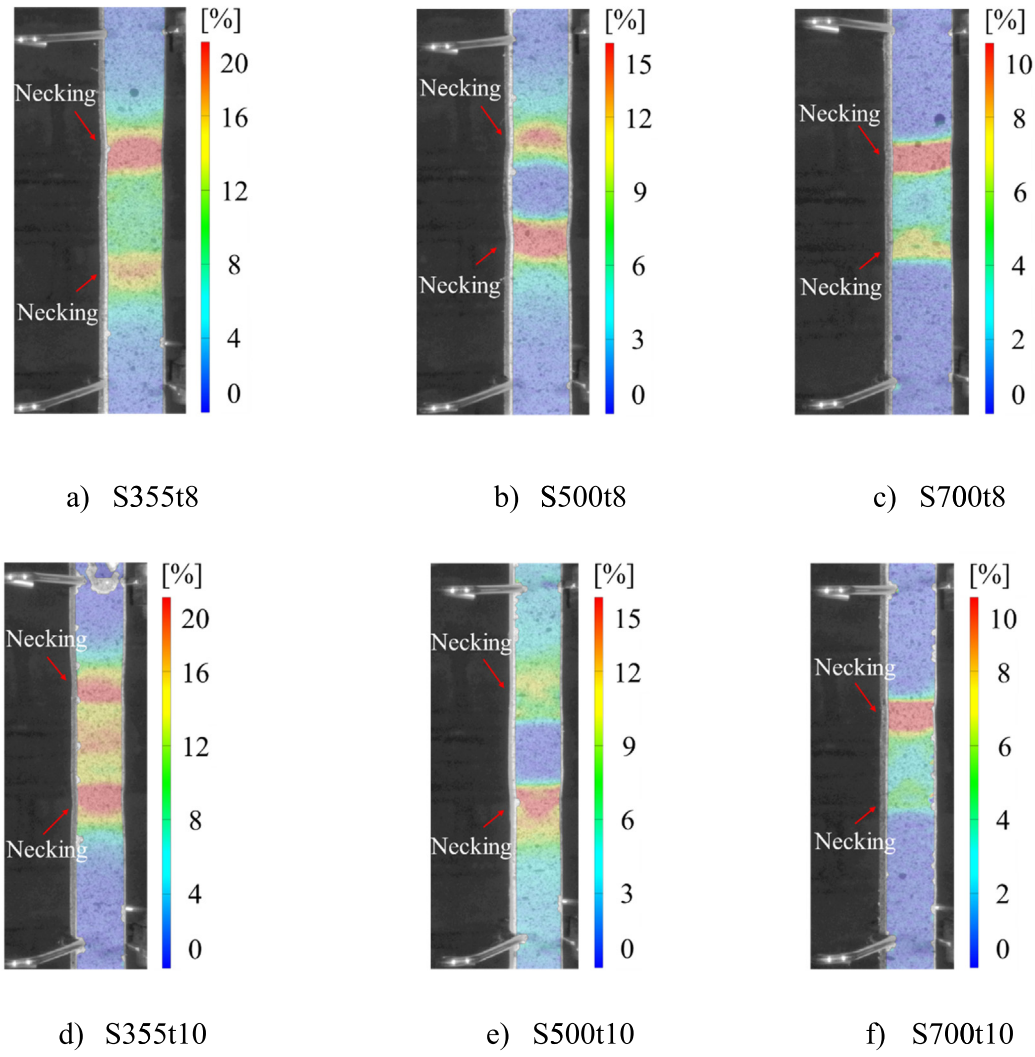

Fig. 5. Contour plots of the major strain at the ultimate load.

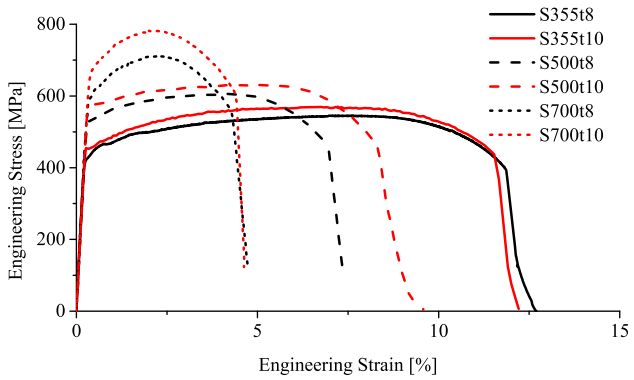

Fig. 6. Engineering stress–strain relationships of the welded coupons.

3 mm, respectively, which are identical to the milled dimensions of the tested specimen. A 0.5 mm fine mesh is used except for the outer edges in the Y direction, "far" from the centre, where 2 mm coarse mesh is used, as shown in Fig. 9. Two material properties, namely the Strong and Weak material, are used in the model. The mechanical properties are presented in Table 7. The only difference between these two materials is that the Weak material has a 100 MPa lower ultimate true stress than the Strong material. The MPC beam constraint is applied to constrain the end surface to a reference point at its centre by all degrees of freedom. The load is applied by a 30 mm displacement at RP2 in the Y direction. The remaining displacement degree of freedom at RP1 and RP2 is fully constrained.

The strain ratio is calculated based on the average strain of elements in three rows for each cross section, shown as the solid red squares in Fig. 9. The strain ratio is plotted against the distance from the regions' boundary in the middle. It can be seen that the strain ratio smaller and larger than −0.5 exists in the vicinity of the Strong and Weak regions' boundary. With the cross-section away from the regions' boundary, the strain ratio gradually approaches −0.5, indicating that the constraint from the adjacent region is disappearing at a certain distance from the boundary.

3.5. Transverse constraint at the boundary of regions

The tested welded coupon consists of five regions in series, resulting in four boundaries, as presented in Fig. 10. Due to the heterogeneity in the grain size of two adjacent regions, transverse constraints in X and Z directions exist at the boundary. Take the BM and HAZ boundary, for instance. BM is stronger than HAZ. Consequently, BM has a less transverse deformation than HAZ during the tensile test, indicating that BM tends to resist the transverse deformation of HAZ at the boundary due to the continuity of the

Table 6
Comparison of mechanical properties obtained from the base material and welded coupons.

Code-name	Base material coupon		Welded coupon	
	Yield strength [MPa]	Tensile strength [MPa]	Yield strength [MPa]	Tensile strength [MPa]
S355t8	506	536	442	545
S355t10	506	539	456	570
S500t8	580	617	534	607
S500t10	593	630	576	632
S700t8	789	861	615	711
S700t10	830	902	688	781

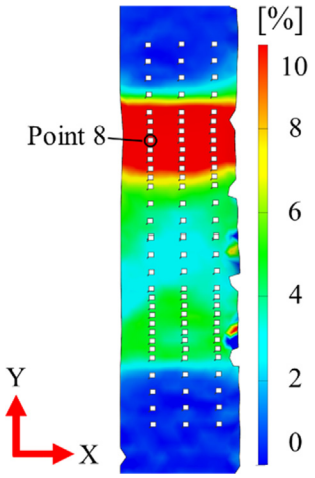

Fig. 7. Measuring points on specimen S700t10 in DIC.

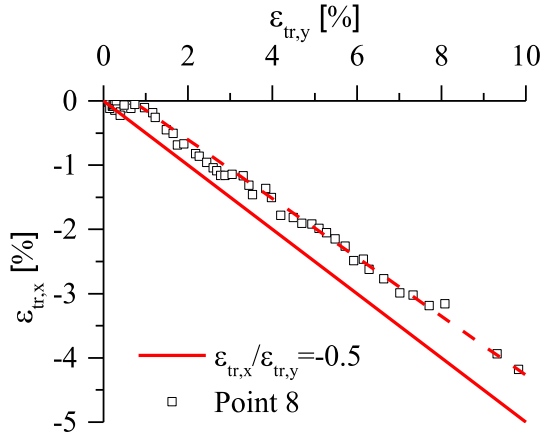

Fig. 8. $\varepsilon_{tr,x}$ - $\varepsilon_{tr,y}$ relationship of Point 8 in HAZ during the loading.

material. Accordingly, the HAZ longitudinal deformation in the loading direction is reduced.

Since the thickness of the tested specimen is only 3 mm, a limited constraint is expected in the thickness direction [6,19]. Hence, the out of plane deformation ($\varepsilon_{tr,z}$) is independent of the constraint at the boundary. Equation (1) is rewritten as:

$$\frac{\varepsilon_{tr,x}}{\varepsilon_{tr,y}} = -1 - \frac{\varepsilon_{tr,z}}{\varepsilon_{tr,y}} \quad (2)$$

From Equation (2), it can be seen that the strain ratio decreases with the increase of the major true strain $\varepsilon_{tr,y}$, given the independent out of plane deformation. The HAZ major strain is smaller at the boundary than the middle of HAZ due to the transverse constraint of BM. Hence, a relatively larger strain ratio is expected in HAZ closing to the boundary than in the other regions. On the contrary, HAZ would increase the strain of BM at the boundary. Consequently, a relatively smaller strain ratio is expected in BM closing to the boundary than in the other regions. The more significant the hardness difference between BM and HAZ, the greater the strain ratio difference.

Based on FEA results in Section 3.4, a conceptual strain ratio plot for a simplified coupon satisfying the three assumptions mentioned above is presented in Fig. 10 a). However, the assumptions do not hold so distinctly in different regions of a real welded specimen. Therefore, Fig. 10 b) depicts the strain ratio distribution closer to the physical evidence.

In Fig. 10 b), the first two assumptions are modified to: 1) the length of HAZ is not sufficient to allow for the vanishment of the boundary constraint; and 2) the hardness measurements difference only exists between WM and HAZ, while the last assumption remains as in the simplified model. Because of limits in the length of HAZ, the strain ratio cannot decrease to −0.5 in the middle of HAZ. The hardness difference between HAZ and BM is relatively small. BM cannot impose a strong transverse constraint on HAZ. Hence, the strain ratio in HAZ is still large at the boundary of WM and HAZ but gradually decreases to −0.5 with a minor increase at the boundary of HAZ and BM. If the hardness transition from HAZ to BM is very smooth, the minor increase of the strain ratio may not exist. A close to "V" shape or a "Monotonic" shape of the strain ratio distribution could be observed in HAZ. These hypotheses are verified by the experimental evidence, as shown in the following sections.

3.6. Comparison of the hardness and the strain ratio results

The strain ratio is examined for all the "white points" shown in Fig. 7. Three points are measured in each cross section. The average strain ratio of each cross section is compared to the hardness results in Fig. 11. Since the coupon specimens were milled to the centre region of 3 mm thickness, the presented hardness results only include Line 2 and Line 3, as shown in Fig. 3. The HAZ regions determined by the strain ratio are shown as the grey stripes with a red dash box, see Fig. 11.

3.6.1. S355 coupons (matching weld)

HAZ in S355 coupons has the weak-weak boundary constraint, as demonstrated in Table 5. Fig. 11 a) and b) show that the variation of the strain ratio in the whole range is relatively small compared to S500 and S700. A typical strain ratio distribution in WM, referring to Fig. 10, is observed in the S355 coupons. The strain ratio is around −0.5 in the middle of WM and slightly decreased at the boundary. A high strain ratio exists in HAZ close to the WM boundary. Hence, the boundary of HAZ and WM is identified between the highest ratio point in HAZ and the lowest ratio point in WM. The point next to the highest ratio point is determined as the boundary. The boundary of HAZ and BM does not show a significant discrepancy in the strain ratio plot because the hardness transition is relatively smooth from HAZ to BM. Hence, the HAZ and BM boundary is identified by the point where the strain ratio

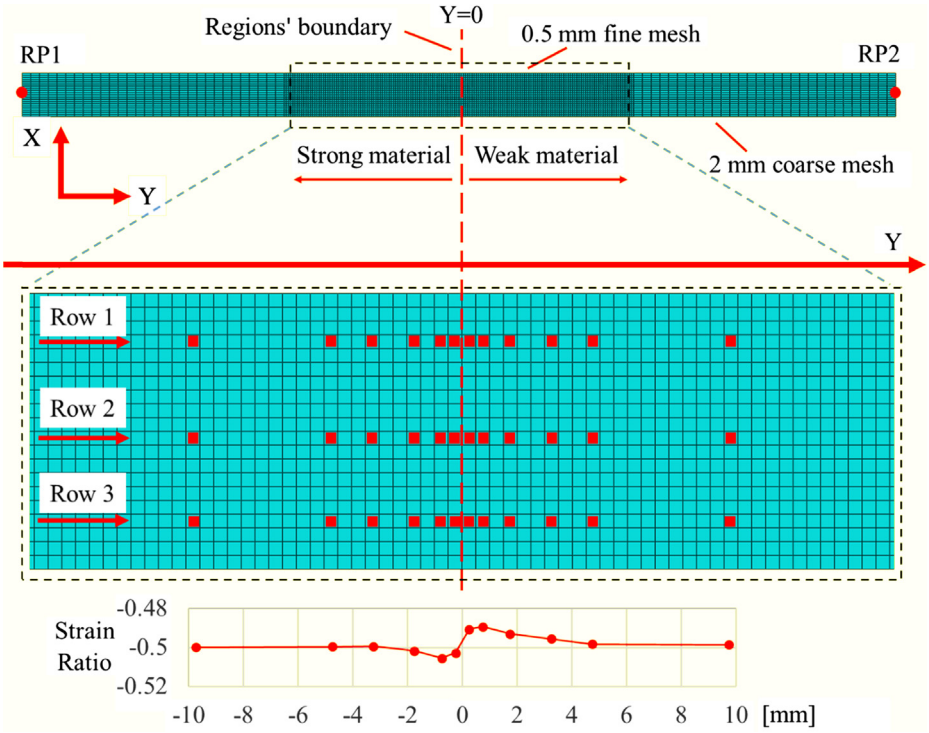

Fig. 9. Results of FEA using the Strong and Weak material connected in series.

Table 7
Mechanical property of a Strong and Weak material.

Material	E [MPa]	f_y [MPa]	$\sigma_{t,u}$ [MPa]	$\varepsilon_{t,u}$ [%]
Strong	200,000	500	1000	20
Weak	200,000	500	900	20

where E is Young's modulus; f_y is the yield strength; $\sigma_{t,u}$ is the ultimate true strength; $\varepsilon_{t,u}$ is the ultimate true strain.

is on the average level of BM. Therefore, two shapes of the strain ratio distribution for HAZ, which are the "Monotonic" shape in S355t8 and "V" shape in S355t10, are characterised.

3.6.2. S500 coupons (overmatching weld)

Fig. 11 c) and d) demonstrate the results of S500 coupons. Since WM is much stronger than HAZ, a significant constraint effect are observed in HAZ close to WM. The boundary of HAZ and WM is identified accordingly. Similar to S355 coupons, the hardness of HAZ and BM are very close. The strain ratio does not show a distinct variation at the boundary. Therefore, it is identified by the point where the strain ratio is on the average level as BM.

Additionally, the strain ratio is missing (not reliable) in a part of WM. According to the hardness results in Table 5, WM is much stronger than HAZ, resulting in smaller major strain (around 0.3%) developing in WM at the ultimate load. The deformation is too small to generate a trend line similar to one shown in Fig. 8,

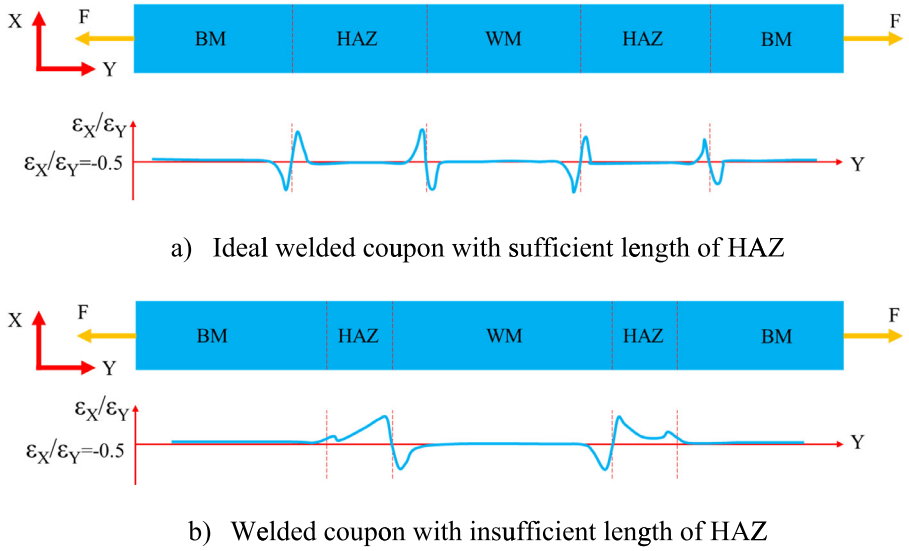

Fig. 10. Strain ratio distribution along with the welded coupon.

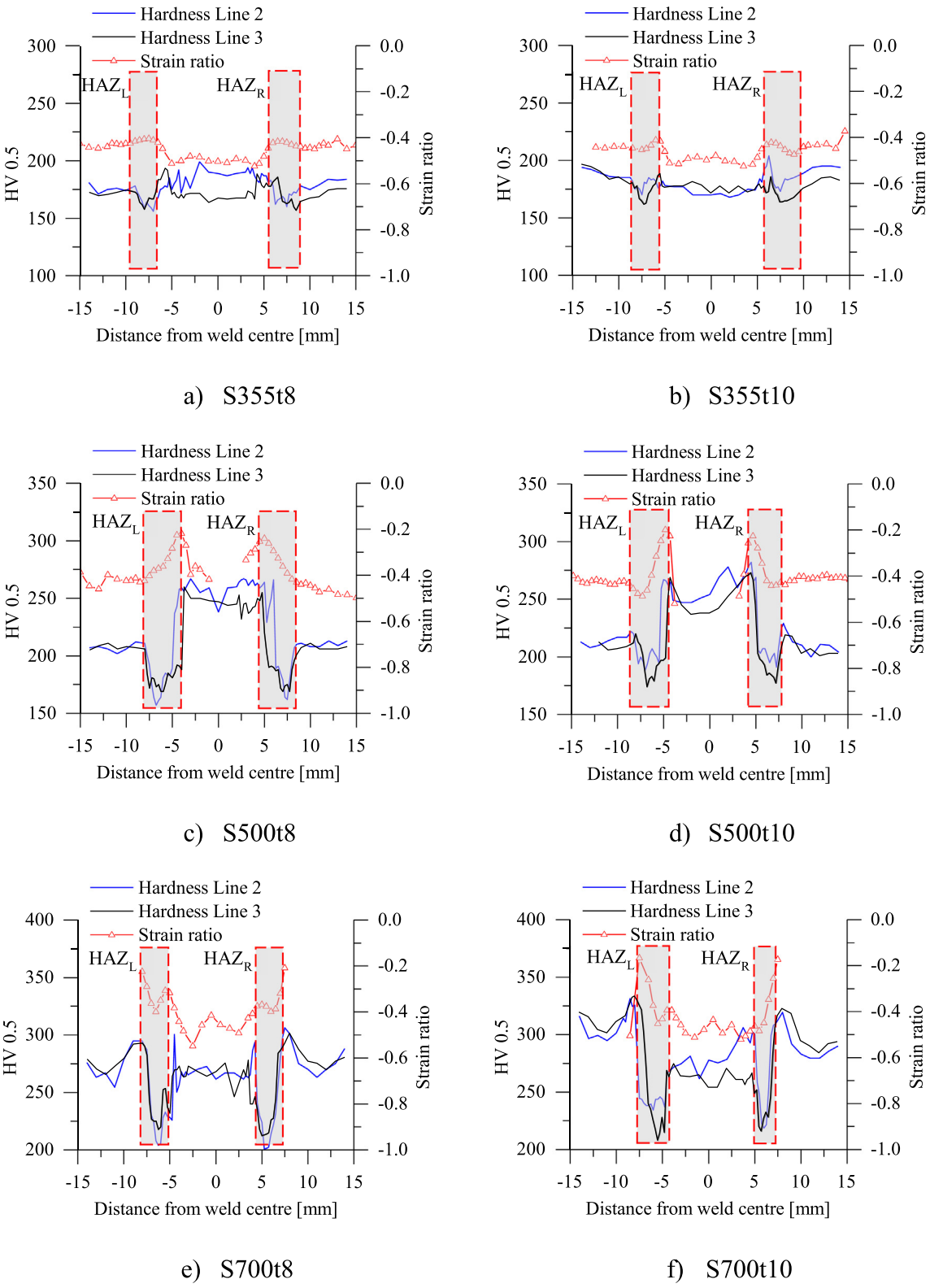

Fig. 11. Comparison of the hardness and the strain ratio results.

considering the actual accuracy of DIC. Hence, the strain ratio could not be calculated.

3.6.3. S700 coupons (undermatching weld)

BM and WM are much stronger than HAZ in S700 coupons. Due to the significant hardness difference, a pronounced boundary constraint effect is observed in the strain ratio plot, and the boundary of HAZ is identified accordingly. A "V" shape strain ratio distribution is observed in both specimens. Besides, the strain ratio in BM cannot be processed for the same reason as WM in S500 coupons.

To summarise, from Fig. 11, it is clear that a good correlation exists between the strain ratio and the hardness results. The HAZ region identified by the strain ratio matches the low hardness

Table 8
Comparison of HAZ width determined by the hardness test and the strain ratio.

Code-name	HAZ_L [mm]			HAZ_R [mm]		
	Hardness	Strain ratio	difference	Hardness	Strain ratio	difference
S355t8	3.3	3.0	0.3	3.6	3.5	0.1
S355t10	3.3	3	0.3	3.6	4	0.4
S500t8	4.0	4.0	0.0	3.9	4.0	0.1
S500t10	3.6	4.0	0.4	3.6	3.5	0.1
S700t8	2.9	3.0	0.1	3.1	3.0	0.1
S700t10	3.5	3.5	0.0	2.4	2.5	0.1

region well. A "V" shape or a "Monotonic" shape of the strain ratio distribution exists in the determined HAZ region. The widths of left and right HAZ (HAZ_L and HAZ_R) determined by the hardness and the strain ratio are compared in Table 8. Note that the hardness result is the average of two widths determined by two indentation lines. An absolute value of the width difference is calculated for each HAZ. The maximum and average differences are 0.4 mm and 0.2 mm, respectively. Therefore, it is concluded that a satisfactory result is obtained using the strain ratio method, and the proposed method could identify the boundary of regions. Note that it is possible to improve the accuracy of the strain ratio results if a smaller interval (smaller than 0.5 mm) is adapted, as presented in Fig. 7. A smaller interval requires smaller facet and step sizes, consequently a higher imaging resolution and a finer speckle size.

The final issue, regarding the repeatability of the experiment, should be addressed since only one welded coupon was tested for each profile. Generally, HAZ may have a similar material scattering as the BM, making it necessary to test many specimens for determining the material property. Strictly interpreting experimental results, it is not sufficient to obtain the material property based on one test for each profile. However, the main purpose of the paper is to propose a methodology for determining the regions' boundary in a coupon with the strong and weak materials connected in series, rather than to investigate specific characteristics of the regions for various steel grades. Although HAZ material scatters, the specimens still follow that HAZ is weaker than BM and WM. Because the proposed method works for the situation where the strong and weak materials are connected in series regardless of the specific strength of HAZ, the HAZ material scattering does not influence the results. In addition, two specimens were tested for each steel grade/matching type. The experiments are repeated from the steel grade perspective, and the HAZ boundary could be identified in both specimens for each steel grade.

4. Conclusions and future work

Six milled coupons with a transverse butt weld in the middle were tested in tension. The hardness and the microstructure were evaluated via the low-force Vickers hardness test (HV 0.5) and the digital optical microscope. The boundary of regions is determined by the hardness and the microstructure results. A method for identifying the boundary of regions using DIC measurements is proposed. The slope of the minor true strain-major true strain relationship in the stage beyond the yield strain, also called the strain ratio for simplicity, is used to distinguish the transverse constraint at the boundary. Finally, the determined HAZ width using the strain ratio approach is verified by the hardness results. The determined HAZ width will be considered in generating material properties relevant for Finite Element Analysis (FEA) of welded joints. Finally, to summarise, the following conclusions are derived:

1) The transverse constraint at the boundary of two regions could be identified by comparing the strain ratio, considering a thin plate (3 mm) assuming almost no constraint in the thickness direction. The strain ratio on the strong side is smaller than that on the weak side. The strain ratio difference between the strong and weak sides has a positive correlation to the hardness difference. Among the tested specimens, the strain ratio difference is less distinct if the hardness difference between two regions is equal to or smaller than 37, indicating that the proposed method is more suitable for the welded high strength steel where a severe strength reduction exists in HAZ.
2) The strain ratio in HAZ has a close to "V" shape or "Monotonic" shape distribution. The starting and the ending points correspond to the HAZ boundaries constrained the most by WM and BM.
3) The HAZ region determined by the strain ratio method shows a good agreement with the hardness results, accompanying 0.4 mm maximum and 0.2 mm average absolute deviation.

In future work, the proposed method, accompanying the tensile coupon test for specimen with a butt weld in the middle, will be used to establish stress–strain relationships for HAZ and WM based on the virtual extensometer with the identified gauge length. The established stress–strain relationship will be validated by FEA.

CRediT authorship contribution statement

Rui Yan: Conceptualization, Data curation, Formal analysis, Methodology, Investigation, Software, Validation, Visualization, Writing - original draft, Writing - review & editing. **Hagar El Bamby:** Data curation, Formal analysis, Writing - review & editing. **Milan Veljkovic:** Conceptualization, Supervision, Writing - review & editing. **Haohui Xin:** Writing - review & editing. **Fei Yang:** Writing - review & editing.

Declaration of Competing Interest

The authors declare that they have no known competing financial interests or personal relationships that could have appeared to influence the work reported in this paper.

Acknowledgements

The authors would like to thank Dr. Kristo Mela (Assist. Prof. at Tampere University) and the company SSAB for their support during this investigation.

Appendix A. Comparison of HV 0.5 hardness and microstructure results

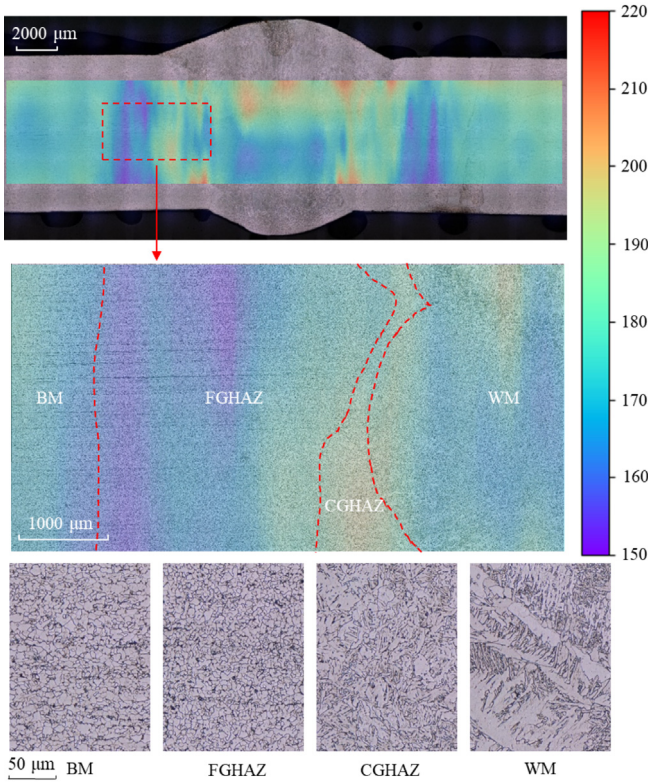

a) Contour plot of HV 0.5 hardness results and microstructures of S355t8

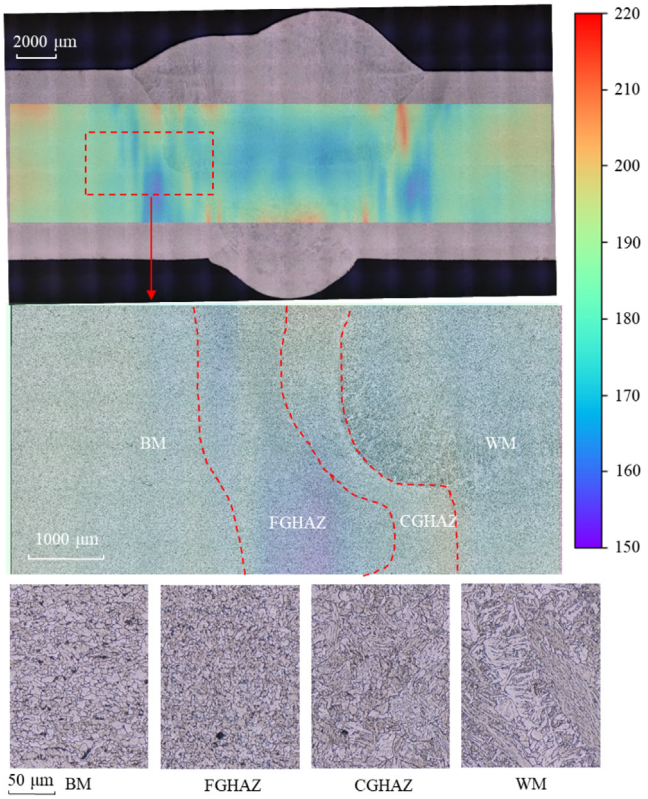

b) Contour plot of HV 0.5 hardness results and microstructures of S355t10

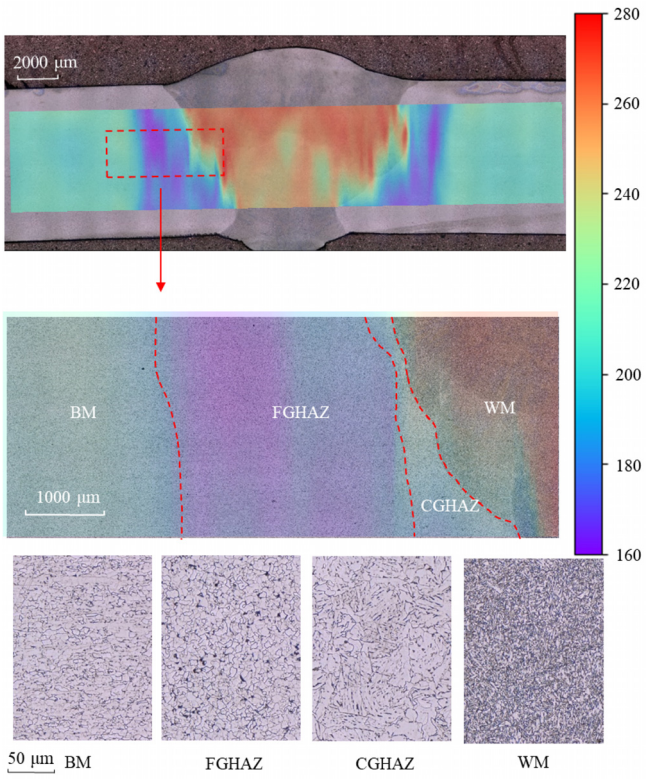

c) Contour plot of HV 0.5 hardness results and microstructures of S500t8

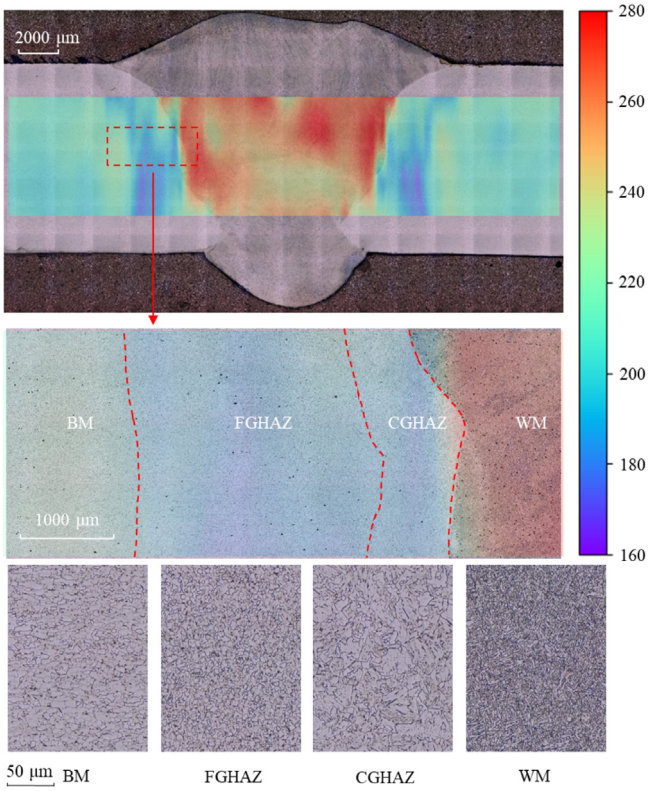

d) Contour plot of HV 0.5 hardness results and microstructures of S500t10

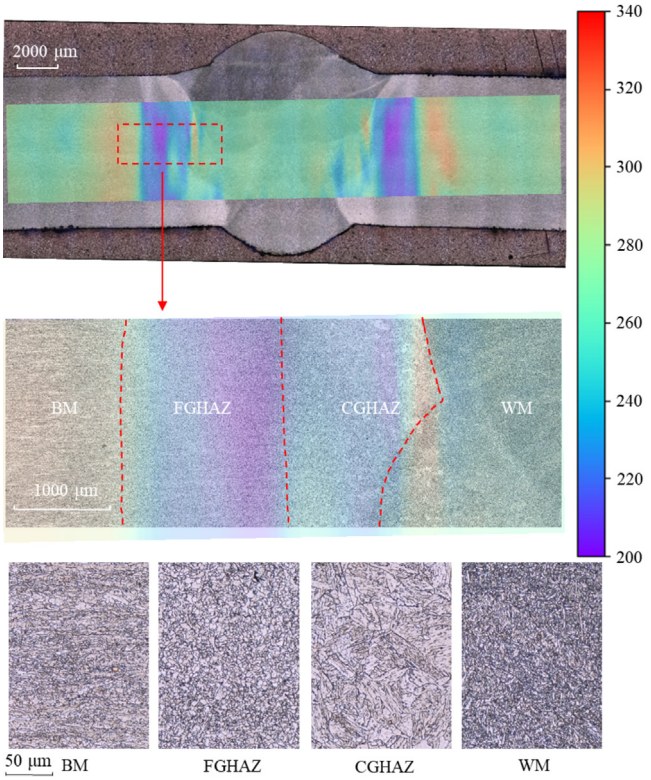

e) Contour plot of HV 0.5 hardness results and microstructures of S700t8

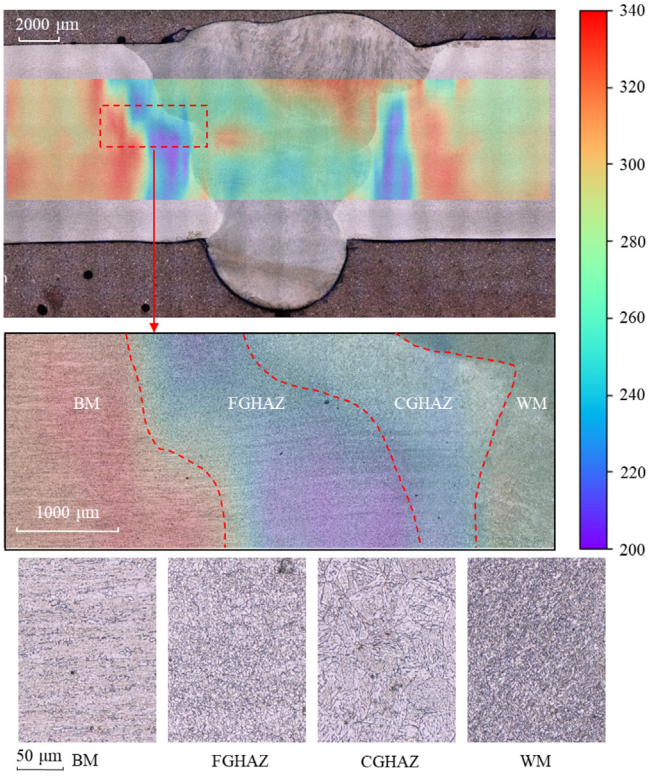

f) Contour plot of HV 0.5 hardness results and microstructures of S700t10

Data availability

The raw/processed data required to reproduce these findings cannot be shared at this time as the data is using by an ongoing study.

References

[1] A. Khalfallah, Experimental and numerical assessment of mechanical properties of welded tubes for hydroforming, Mater. Des. 56 (2014) 782–790, https://doi.org/10.1016/j.matdes.2013.11.051.

[2] M.-L. Zhu, F.-Z. Xuan, Correlation between microstructure, hardness and strength in HAZ of dissimilar welds of rotor steels, Mater. Sci. Eng., A 527 (16-17) (2010) 4035–4042, https://doi.org/10.1016/j.msea.2010.03.066.

[3] Y. Peng, C. Wu, J. Gan, J. Dong, Characterization of heterogeneous constitutive relationship of the welded joint based on the stress-hardness relationship using micro-hardness tests, Constr. Build. Mater. 202 (2019) 37–45, https://doi.org/10.1016/j.conbuildmat.2018.12.218.

[4] A. Considère, Annales des Ponts et Chaussées 9 (1885) 574–775.

[5] H. Hollomon, Tensile deformation, Aime Trans. 12 (1945) 1–22.

[6] C. Leitão, I. Galvão, R.M. Leal, D.M. Rodrigues, Determination of local constitutive properties of aluminium friction stir welds using digital image correlation, Mater. Des. 33 (2012) 69–74, https://doi.org/10.1016/j.matdes.2011.07.009.

[7] D. Tabor, The Hardness of Metals, Oxford University Press, 1951.

[8] M. Amraei, S. Afkhami, V. Javaheri, J. Larkiola, T. Skriko, T. Björk, X.-L. Zhao, Mechanical properties and microstructural evaluation of the heat-affected zone in ultra-high strength steels, Thin-Walled Struct. 157 (2020) 107072, https://doi.org/10.1016/j.tws.2020.107072.

[9] R.M. Molak, K. Paradowski, T. Brynk, L. Ciupinski, Z. Pakiela, K.J. Kurzydlowski, Measurement of mechanical properties in a 316L stainless steel welded joint, Int. J. Press. Vessels Pip. 86 (1) (2009) 43–47, https://doi.org/10.1016/j.ijpvp.2008.11.002.

[10] J. Kim, Y.-W. Kim, B.-S. Kang, S.-M. Hwang, Finite element analysis for bursting failure prediction in bulge forming of a seamed tube, Finite Elem. Anal. Des. 40 (2004) 953–966, https://doi.org/10.1016/j.

[11] M. Flansbjer, T. Sjögren, Using digital image correlation techniques and finite element models for strain-field analysis of a welded aluminium structure, Appl. Mech. Mater. 70 (2011) 123–128, https://doi.org/10.4028/www.scientific.net/AMM.70.123.

[12] C. Chen, S.P. Chiew, M.S. Zhao, C.K. Lee, T.C. Fung, Welding effect on tensile strength of grade S690Q steel butt joint, J. Constr. Steel Res. 153 (2019) 153–168, https://doi.org/10.1016/j.jcsr.2018.10.009.

[13] C. Chen, S.-P. Chiew, M.-S. Zhao, C.-K. Lee, T.-C. Fung, Influence of cooling rate on tensile behaviour of S690Q high strength steel butt joint, J. Constr. Steel Res. 173 (2020) 106258, https://doi.org/10.1016/j.jcsr.2020.106258.

[14] M. Amraei, T. Skriko, T. Björk, X.L. Zhao, Plastic strain characteristics of butt-welded ultra-high strength steel (UHSS), Thin-Walled Struct. 109 (2016) 227–241, https://doi.org/10.1016/j.tws.2016.09.024.

[15] F. Farrokhi, J. Siltanen, A. Salminen, Fiber laser welding of direct-quenched ultrahigh strength steels: evaluation of hardness, tensile strength, and toughness properties at subzero temperatures, journal of manufacturing science and engineering, Trans. ASME. 137 (2015) 1–10, https://doi.org/10.1115/1.4030177.

[16] R. Stroetmann, T. Kästner, A. Hälsig, P. Mayr, Influence of the cooling time on the mechanical properties of welded HSS-joints, Steel Constr. 11 (2018) 264–271, https://doi.org/10.1002/stco.201800019.

[17] A.P. Reynolds, F. Duvall, Digital image correlation for determination of weld and base metal constitutive behavior, Welding J. (Miami, Fla) 78 (1999) 355-s.

[18] W.D. Lockwood, B. Tomaz, A.P. Reynolds, Mechanical response of friction stir welded AA2024: experiment and modeling, Mater. Sci. Eng., A 323 (1-2) (2002) 348–353, https://doi.org/10.1016/S0921-5093(01)01385-5.

[19] W.D. Lockwood, A.P. Reynolds, Simulation of the global response of a friction stir weld using local constitutive behavior, Mater. Sci. Eng., A 339 (1-2) (2003) 35–42, https://doi.org/10.1016/S0921-5093(02)00116-8.

[20] M.A. Sutton, J.H. Yan, S. Avril, F. Pierron, S.M. Adeeb, Identification of heterogeneous constitutive parameters in a welded specimen: uniform stress and virtual fields methods for material property estimation, Exp. Mech. 48 (4) (2008) 451–464, https://doi.org/10.1007/s11340-008-9132-6.

[21] R. Bai, Y. Wei, Z. Lei, H. Jiang, W. Tao, C. Yan, X. Li, Local zone-wise elastic-plastic constitutive parameters of Laser-welded aluminium alloy 6061 using digital image correlation, Opt. Lasers Eng. 101 (2018) 28–34, https://doi.org/10.1016/j.optlaseng.2017.09.023.

[22] X. Wu, J. Shuai, K. Xu, Z. Lv, Local constitutive behavior of undermatched welded joints in pipeline steel using digital image correlation technology, J. Pressure Vessel Technol., Trans. ASME. 142 (2020) 1–6, https://doi.org/10.1115/1.4047271.

[23] Y. Peng, C. Wu, J. Gan, J. Dong, Determination of the local constitutive properties of the welded steel joints using digital image correlation method, Constr. Build. Mater. 171 (2018) 485–492, https://doi.org/10.1016/j.conbuildmat.2018.03.182.

[24] G. Li, F. Xu, G. Sun, Q. Li, Identification of mechanical properties of the weld line by combining 3D digital image correlation with inverse modeling procedure, Int. J. Adv. Manuf. Technol. 74 (5-8) (2014) 893–905, https://doi.org/10.1007/s00170-014-6034-x.

[25] M.I. Costa, D.M. Rodrigues, C. Leitão, Analysis of AA 6082–T6 welds strength mismatch: stress versus hardness relationships, Int. J. Adv. Manuf. Technol. 79 (5-8) (2015) 719–727, https://doi.org/10.1007/s00170-015-6866-z.

[26] W.H. Peters, W.F. Ranson, Digital imaging techniques in experimental stress analysis Digital imaging techniques in experimental stress analysis (1982).

[27] Metallic materials - Tensile testing - Part 1: Method of test at room temperature (ISO 6892-1:2019), 1 (2019).

[28] NEN-EN-ISO 6507-1 Metallic materials - Vickers hardness test - Part 1: Test method 1 (2018).

[29] NEN-EN-ISO 6507-4 Metallic materials - Vickers hardness test - Part 4: Tables of hardness values 4 (2018).

[30] P. Reu, All about speckles: speckle size measurement, Exp. Tech. 39 (2014) 1–2, https://doi.org/10.1111/ext.12161.

[31] P. Reu, All about speckles: aliasing, Exp. Tech. 38 (2014) 1–3, https://doi.org/10.1111/ext.12111.

[32] M.A. Sutton, J.-J. Orteu, H.W. Schreier, Image correlation for shape, motion and deformation measurements, 2009.

[33] D. Wojnowski, Y.K. Oh, J.E. Indacochea, Metallurgical assessment of the softened HAZ region during multipass welding, J. Manuf. Sci. Eng., Trans. ASME. 122 (2000) 310–315, https://doi.org/10.1115/1.538920.

[34] ABAQUS, Abaqus Analysis User's Manual, 2019 version (2019).